Length scales, patterns and origin of azimuthal seismic anisotropy in the upper mantle as mapped by Rayleigh waves

Thorsten W. Becker,[1] Göran Ekström,[2] Lapo Boschi[3] and John H. Woodhouse[4]

[1]*Department of Earth Sciences, University of Southern California, 3651 Trousdale Parkway, Los Angeles CA 90089-0740, USA. E-mail: twb@usc.edu*
[2]*Department of Earth and Environmental Sciences, Lamont-Doherty Earth Observatory, Palisades, NY 10964, USA*
[3]*Eidgenössische Technische Hochschule, Zürich, Switzerland*
[4]*Department of Earth Sciences, University of Oxford, Parks Road, Oxford OX1 3PR, UK*

SUMMARY
We measure the degree of consistency between published models of azimuthal seismic anisotropy from surface waves, focusing on Rayleigh wave phase-velocity models. Some models agree up to wavelengths of ∼2000 km, albeit at small values of linear correlation coefficients. Others are, however, not well correlated at all, also with regard to isotropic structure. This points to differences in the underlying data sets and inversion strategies, particularly the relative 'damping' of mapped isotropic versus anisotropic anomalies. Yet, there is more agreement between published models than commonly held, encouraging further analysis. Employing a generalized spherical harmonic representation, we analyse power spectra of orientational (2Ψ) anisotropic heterogeneity from seismology. We find that the anisotropic component of some models is characterized by stronger short-wavelength power than the associated isotropic structure. This spectral signal is consistent with predictions from new geodynamic models, based on olivine texturing in mantle flow. The flow models are also successful in predicting some of the seismologically mapped patterns. We substantiate earlier findings that flow computations significantly outperform models of fast azimuths based on absolute plate velocities. Moreover, further evidence for the importance of active upwellings and downwellings as inferred from seismic tomography is presented. Deterministic estimates of expected anisotropic structure based on mantle flow computations such as ours can help guide future seismologic inversions, particularly in oceanic plate regions. We propose to consider such *a priori* information when addressing open questions about the averaging properties and resolution of surface and body wave based estimates of anisotropy.

**Key words:** mantle convection, seismic anisotropy, surface waves.

GJI Tectonics and geodynamics

1 INTRODUCTION

The Earth's upper mantle is seismically anisotropic (e.g. Hess 1964; Forsyth 1975; Anderson & Dziewoński 1982; Vinnik *et al.* 1989; Montagner & Tanimoto 1991) and particularly azimuthal anisotropy is often used to infer mantle flow from seismological observations (e.g. Tanimoto & Anderson 1984). It is therefore, important to understand the degree of robustness in mapped patterns before increasing geodynamic model complexity. Here, we focus on azimuthal anisotropy from Rayleigh waves and analyse the match between geodynamic and seismological models, as well as their spectral character.

Imaging azimuthal anisotropy is notoriously complicated and affected by issues such as the trade-off between isotropic and anisotropic structure (e.g. Tanimoto & Anderson 1985; Larsen *et al.* 1998; Laske & Masters 1998), required regularization choices for additional parameters compared to isotropic inversions (e.g. Zhang

& Lay 1996; Trampert & Woodhouse 2003), and finite frequency wave propagation effects (e.g. Smith *et al.* 2004; Sieminski *et al.* 2007). While trade-offs between isotropic and anisotropic patterns are probably small for large-scale patterns provided that azimuthal coverage is good (Montagner & Jobert 1988), relative amplitudes are strongly sensitive to the damping choices.

However, several models of global, upper-mantle azimuthal structure have recently been published (Montagner & Guillot 2000; Ekström 2001; Trampert & Woodhouse 2003; Debayle *et al.* 2005; Beucler & Montagner 2006) with some consistent, apparently plate-tectonics related features (Fig. 1). Moreover, deterministic geodynamic modelling has been successful in explaining at least part of the signal based on mantle flow (e.g. Becker *et al.* 2003; Gaboret *et al.* 2003; Behn *et al.* 2004). This suggests that further study is needed to tease out in which regions, and on what spatial scales, features can be used to infer information about the detailed dynamics of mantle convection.
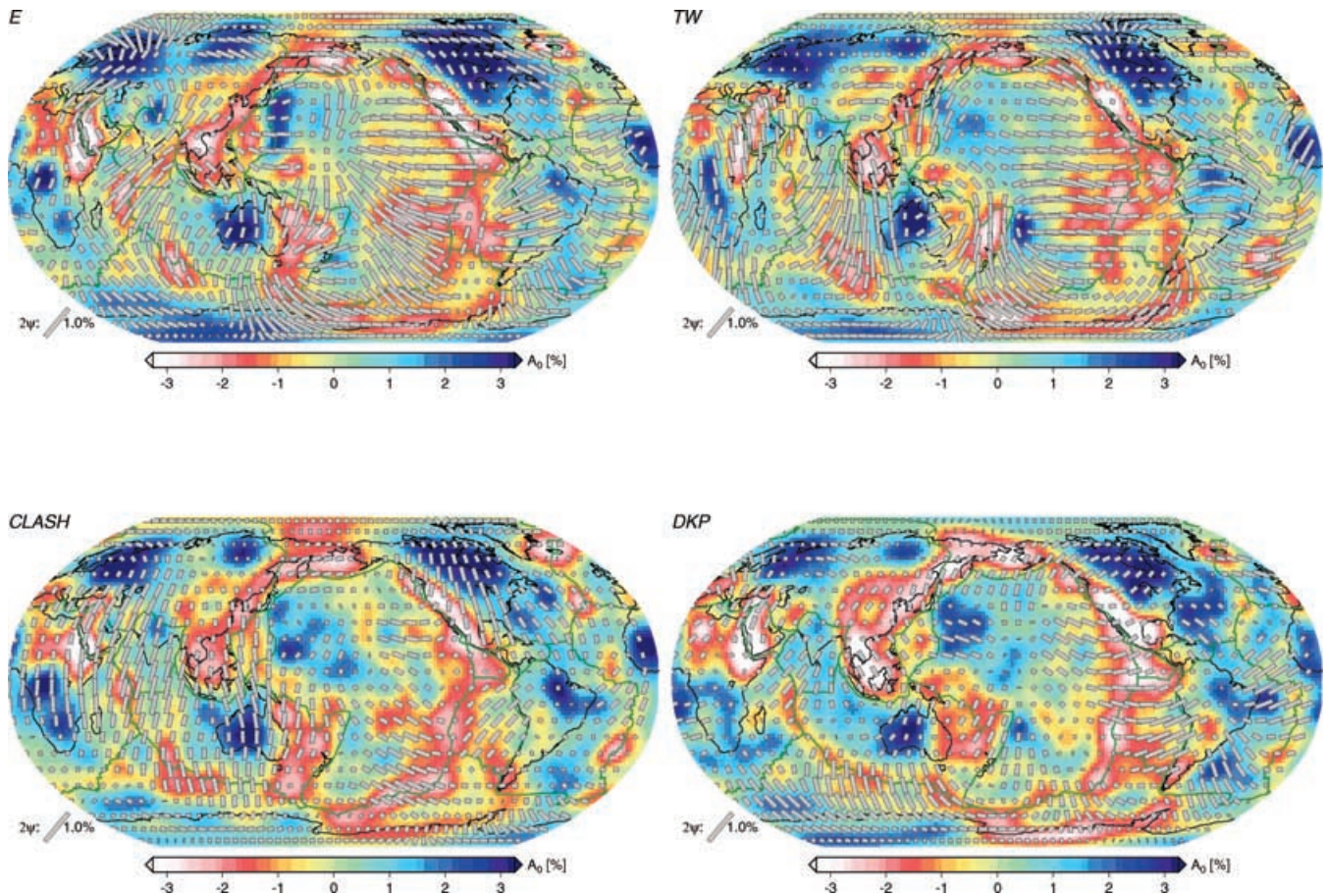
Figure 1. Comparison of published surface wave anisotropy estimates for Rayleigh wave anomalies at 100 s period (peak sensitivity at ∼110 km depth). Background shading is the isotropic anomaly (mean removed), A_0, with respect to PREM (Dziewoński & Anderson 1981) expanded up to spherical harmonic degree $L = 20$. Grey sticks indicate the azimuthal, 2Ψ, component (see eq. 1), and legend for scaling), expanded up to $L = 8$. Models: *E*: Ekström (2001), *TW*: Trampert & Woodhouse (2003), *CLASH*: Beucler & Montagner (2006) and *DKP*: Debayle *et al.* (2005) (kernel averaged from the original 3-D model, including 3SMAC (Nataf & Ricard 1996) crustal layer for A_0), see Table 1.

It is clearly desirable to advance wave propagation theory and analyse modelling choices such as data selection, parametrization, and damping by means of evaluating inferred structure based on the different data sets with consistent inversion strategies. Here, however, we present a preliminary step, an analysis of the similarity between published models and the degree of mapped and expected surface wave heterogeneity. We focus on patterns, rather than amplitudes, of mapped anomalies and defer detailed examination of the types of expected anisotropy to later study.

Some of our findings with regard to the degree of agreement between seismological models are reflected in common notions in the seismological community. However, we provide the first quantitative comparison between modern anisotropic models using the consistent, wavelength-dependent representation that can be achieved using generalized spherical harmonics (Phinney & Burridge 1973; Mochizuki 1986; Trampert & Woodhouse 2003; Boschi & Woodhouse 2006). Importantly, we also provide a physical basis to judge mapped upper mantle heterogeneity. Our goal is not to say which model is 'better' than another, as such statements always depend on subjective choices and the questions asked. Rather, we wish to obtain insights in the characteristics of different models before they are used as input for geodynamic studies.

2 METHODS

In a half-space, perturbations to phase velocity c due to general, but small anisotropy can be expressed as a series of isotropic, π-periodic and $\pi/2$ periodic terms (Smith & Dahlen 1973, 1975):

$$\frac{\delta c}{c} \approx A_0 + A_1 \cos(2\Psi) + A_2 \sin(2\Psi)$$
$$+ A_3 \cos(4\Psi) + A_4 \sin(4\Psi). \qquad (1)$$

The A_i factors are model parameters that depend on location, and Ψ is the azimuth of wave propagation. Romanowicz & Snieder (1988) and Larsen *et al.* (1998) showed that the same expansion holds for a spherical Earth, and this formulation is often applied in studies of anisotropy of the upper mantle. We shall refer to the $\{A_1, A_2\}$ and $\{A_3, A_4\}$ terms as '2Ψ' and '4Ψ' anomalies or components, respectively.

On the one hand, we expect a small signal in 4Ψ anomalies for Rayleigh or *SV* waves for lattice preferred (LPO) alignment of olivine (Montagner & Nataf 1986). On the other hand, observational studies have argued for a significant 4Ψ contribution (Trampert & Woodhouse 2003; Beucler & Montagner 2006). Here, we focus on the 2Ψ signal that is generally believed to be better constrained

than 4Ψ (e.g. Ekström 2001; Trampert & Woodhouse 2003) for simplicity.

Isotropic anomalies given on a spatial grid at location j, $A^j{}_0$, are expanded in scalar spherical harmonics (SH), using the physical, ortho-normalized convention of, for example, (Dahlen & Tromp 1998, appendix B.8). We denote harmonic degree and order as l and m, respectively, use real spherical harmonics with $0 \le m \le l$, and limit the expansions to maximum degree L. For A_0, we thus have $N^0_l = 2l + 1$ non-zero SH coefficients per degree for cos and sin terms, which we write as a vector

$$\mathbf{p}^0 = \{p^0_i\} = \{a^0_{lm}, b^0_{lm}\}, \tag{2}$$

and a total of $N^0 = (L+1)^2$ coefficients.

To express the spatial 2Ψ anisotropic anomalies, $\{A^j{}_1, A^j{}_2\}$, in a consistent framework, we employ generalized spherical harmonics (GSH, see, e.g. Dahlen & Tromp 1998, appendix C). GSH were introduced by Mochizuki (1986) for anisotropic Earth parameters; we use the approach of Trampert & Woodhouse (2003) and implementation by Boschi & Woodhouse (2006). For 2Ψ, this means introducing a 2×2 tensor $\boldsymbol{\tau}$

$$\tau_{\theta\theta} = -\tau_{\phi\phi} = A_1 \tag{3}$$

$$\tau_{\theta\phi} = \tau_{\phi\theta} = -A_2. \tag{4}$$

With $\boldsymbol{\nu} = \{-\sin(\Psi), \cos(\Psi)\}$, the 2Ψ terms of eq. (1) can then be written as

$$\frac{\delta c}{c}\Big|_{2\Psi} = A_1 \cos(2\Psi) + A_2 \sin(2\Psi) = \nu_i \nu_j \tau_{ij} = \boldsymbol{\nu}^T \cdot \boldsymbol{\tau} \cdot \boldsymbol{\nu}, \tag{5}$$

where the summation convention applies. Being a tensorial quantity defined on a sphere, $\boldsymbol{\tau}$ is most conveniently parametrized as a linear combination of generalized spherical harmonics (Boschi & Woodhouse 2006). This requires that its contravariant components (e.g. Phinney & Burridge 1973; Dahlen & Tromp 1998, appendix C) τ^{++}, τ^{-+}, τ^{+-} and τ^{--} be introduced; they are related to the θ, ϕ-components of $\boldsymbol{\tau}$ through

$$\tau^{++} = \tau_{\theta\theta} - i\tau_{\theta\phi} \tag{6}$$

$$\tau^{--} = \tau_{\theta\theta} + i\tau_{\theta\phi} \tag{7}$$

while $\tau^{-+} = \tau^{+-} = 0$. Boschi & Woodhouse (2006) show how, thanks to the symmetry properties of $\boldsymbol{\tau}$, its generalized harmonic expansion is limited to second-rank harmonics Y^2_{lm},

$$\tau_{\theta\theta} = \sum_{l=0}^{\infty} \sum_{m=-l}^{l} \big\{ Re\big(\tau^{++}_{lm}\big) Re\big(Y^2_{lm}\big) \\ - Im\big(\tau^{++}_{lm}\big) Im\big(Y^2_{lm}\big) \big\} \tag{8}$$

$$\tau_{\theta\phi} = \sum_{l=0}^{\infty} \sum_{m=-l}^{l} \big\{ -Im\big(\tau^{++}_{lm}\big) Re\big(Y^2_{lm}\big) \\ - Re\big(\tau^{++}_{lm}\big) Im\big(Y^2_{lm}\big) \big\}. \tag{9}$$

The Y^2_{lm} are defined as in Boschi & Woodhouse (2006, appendix A). Our numerical implementation is, however, slightly modified; we scale the A_0 coefficients of their Y_{lm} convention by $1/\sqrt{2}$ for $m \neq 0$, and all 2Ψ terms by $\sqrt{3/4}$ to make the expansions ortho-normalized. As for the A_0 case, the infinite series in eqs (8) and (9) is of course approximated with a finite sum up to L in our practical application below. The real and imaginary parts, Re and Im, of τ^{++}

and Y^2_{lm} are treated as separate, real numbers for computations. We denote the resulting coefficients again as a vector

$$\mathbf{p}^{2\Psi} = \{p^{2\Psi}_i\} = \{a^{2\Psi}_{lm}|_{Re}, a^{2\Psi}_{lm}|_{Im}, b^{2\Psi}_{lm}|_{Re}, b^{2\Psi}_{lm}|_{Im}\}. \tag{10}$$

This yields $N^{2\Psi}_l = 4l + 2$ non-zero coefficients per degree. As $Y^2_{lm} = 0$ for $l < 2$, the total number of coefficients for 2Ψ is $N^{2\Psi} = (2L+6)(L-1)$ (Trampert & Woodhouse 2003).

2.1 Power and correlation

To evaluate the seismological and geodynamic model character in a global sense, it is useful to consider the spectral power of the SH or GSH expansions and their respective correlation. We define the power per degree of a harmonic representation of a spherical Earth model as

$$\sigma_l = \left(\frac{1}{N_l} \sum_{i=1}^{N_l} p^2_i \right)^{\frac{1}{2}}. \tag{11}$$

This expression is valid both for the isotropic (A_0) and the 2Ψ terms: in the first case, $N_l = N^0_l$ and $p_i = p^0_i$; in the second case, $N_l = N^{2\Psi}_l$ and $p_i = p^{2\Psi}_i$.

The linear correlation coefficient at degree l between two harmonic fields $\mathbf{p}$ and $\mathbf{q}$ is defined as

$$r_l = \frac{\sum_{i=1}^{N_l} p_i q_i}{\sqrt{\sum_{i=1}^{N_l} p^2_i} \sqrt{\sum_{i=1}^{N_l} q^2_i}}. \tag{12}$$

The total correlation of two expansions up to degree L, $r(L)$, is computed by replacing N_l with N in eq. (12). To evaluate r values statistically, we assume that the deviations of $\mathbf{p}$ and $\mathbf{q}$ harmonic coefficients from a linear relationship obey a Gaussian distribution. (We have checked the residuals of several such comparisons, and this seems to be adequate.) Standard techniques can then be applied to make approximate statements about the significance of correlations (e.g. Press *et al.* 1993, p. 636f). We further assume that the appropriate number of degrees of freedom for statistics is the number of harmonic coefficients of the GSH expansions because the models under consideration contain spatial information up to the degrees L used for $r(L)$ (see Section 3.1). The level at which correlations r_l are significantly different from random is then given by Student's t-distribution $A(N_l - 2|t)$ (e.g. Press *et al.* 1993, p. 228) with

$$t = r_l \sqrt{\frac{(N_l - 2)}{1 - r^2_l}}, \tag{13}$$

for N_l harmonic coefficients at degree l with $N_l \ll 500$.

After calculating correlations between various combinations of models, and comparing the results, we ask whether differences between the results are significant in a statistical sense. Denoting with r^1 and r^2 two values of (statistically significant, r^1, $r^2 \neq 0$) correlation (e.g. $r(20)$, with $N \gtrsim 500$) that we wish to compare, this is addressed by first applying Fisher's z transformation

$$z(r) = \frac{1}{2} \ln \left(\frac{1+r}{1-r} \right) \tag{14}$$

to each computed r, and then substituting the found value for $z(r)$ into the probability formula

$$p(r^1, r^2) = \text{erfc} \left[\frac{|z(r^1) - z(r^2)| \sqrt{N-3}}{2^y} \right] \tag{15}$$

(e.g. Press *et al.* 1993, p. 637f). Here, erfc denotes the complementary error function, $y \equiv 1$, and N is the number of coefficients to

compare (N_l for our harmonic parametrizations). The $1 - p(r^1, r^2)$ value then describes the level of significance of differences in correlations, under the caveats mentioned above. Also, if r^1 remains a statistically significant non-zero value of correlation, a null hypothesis test can be conducted by replacing y in eq. (15) with $1/2$ and setting $r^2 = 0$.

3 MODELS

3.1 Seismology

We proceed to describe the models we analyse; for a list and abbreviations, see Table 1. Four seismological models of upper mantle azimuthal anisotropy are considered (Fig. 1). The first three, by Ekström (2001) (*E*), Trampert & Woodhouse (2003) (*TW*) and Beucler & Montagner (2006) (*CLASH*) are based on inversions of three different, large surface wave dispersion data sets. We focus on results obtained for Rayleigh wave, fundamental mode phase-velocity. Each inversion solves for A_0, 2Ψ and 4Ψ structure, while employing different parametrization, damping, and reference models. Consistently, anisotropic structure is damped more strongly than isotropic anomalies. Models are parametrized with spherical splines at $\sim 2 \times 2°$ spacing for *E* (Ekström 2006), and generalized spherical harmonics with $L = 40$ for A_0 and $L = 20$ for 2Ψ and 4Ψ for *TW*. Beucler & Montagner (2006) employ a regular pixel parametrization but include lateral variations in resolution by means of ray coverage dependent covariances. We use three periods of phase velocity maps at 50, 100 and 150 s for *E*, *CLASH* and *TW*. (Rayleigh waves at 50 and 150 s seconds show strongest 2Ψ sensitivity at ~ 50 and ~ 200 km depth, respectively.) We convert models, if needed, to δc anomalies with respect to PREM (Dziewoński & Anderson 1981).

The fourth seismological model we consider was published by Debayle *et al.* (2005) and is dubbed *DKP* by us. This study employs a different approach using waveform inversions and a variable resolution parametrization as described in Debayle & Sambridge (2004). *DKP* is a model of three-dimensional (3-D) variations in vertically polarized shear (*SV*) velocity throughout the Earth's upper mantle. We associate 2-D A_0 and 2Ψ structure to *DKP*, calculating its local kernel-weighted averages using Montagner & Nataf's (1986) formulation (see, e.g. Becker *et al.* 2003, appendix for details). For shallow A_0, this conversion incorporates the addition of 3SMAC (Nataf & Ricard 1996) crustal anomalies to *DKP* since Debayle *et al.* (2005) used 3SMAC as a crustal starting model. For simplicity, we use PREM-based kernels, however, and assume that the sensitivity kernels relating heterogeneities in *SV* velocity at depth to the local A_0 term coincide with those relating 2Ψ anisotropy (in *SV*) to the local 2Ψ anisotropy of Rayleigh waves. We compare the *E*, *TW* and *CLASH* surface wave studies with *DKP* as a somewhat

distinct approach to image Earth structure, but expect the first three models to be more similar to each other.

There are significant differences in the phase velocity measurement strategies (Trampert & Woodhouse 1995; Ekström *et al.* 1997; van Heijst & Woodhouse 1999), and the parametrization and damping as used for models *E* and *TW*. In terms of inversion strategy, it is of importance here that *TW* chose to impose strong smoothness constraints on anisotropic patterns following a statistical significance test (section 4 of Trampert & Woodhouse 2003). This leads to a real spectral resolution in 2Ψ for *TW* that is $l \lesssim 10$ by design, less than the nominal resolution of $L = 20$. Beucler & Montagner (2006) have discussed their results in comparison with other models, particularly *TW*. These authors found good visual agreement in A_0 between *TW* and *CLASH*, and some agreement in 2Ψ, though Beucler & Montagner did not explore this further quantitatively.

Here, all models which are not given in SH coefficients are reparametrized into a GSH expansion using least-squares fitting of A_i^j values for the spatial grids on which original model results were shared electronically. We tested that our expansion scheme captures 100 per cent of *TW*, which was originally parametrized as GSH. For most results shown, we use a maximum spherical harmonic degree $L = 20$. This corresponds to the L used for 2Ψ by Trampert & Woodhouse (2003), but we also fit lower degree, $L = 8$, expansions to the 2Ψ terms, as this is closer to *TW*'s real anisotropic model resolution.

Ekström (2001), Beucler & Montagner (2006) and Debayle *et al.*'s (2005) models contain a small degree of power at wavelengths shorter than $L = 20$ in both isotropic and anisotropic model structure. We define the variance reduction of the GSH description of irregular models as

$$VR = 1 - \chi^2 / |\mathbf{A}|^2, \tag{16}$$

where χ^2 is the misfit between original and GSH $\mathbf{A} = \{A_i^j\}$ parameters. The *VR* values for two periods in Table 2 give an impression of the spectral character of these models. With the *VR* metric, $\gtrsim 90$ per cent of all structure in *E*, *CLASH* and *DKP* is within $l \leq 20$. As the better fit to A_0 than to 2Ψ for $L = 8$ shows, isotropic patterns in *E* and *DKP* have relatively more long-wavelength power than the anisotropic signal. This difference is more pronounced for 4Ψ, for both *CLASH* and *E*.

3.2 Geodynamics

Following the method of Becker *et al.* (2003, 2006a), we use flow models to predict the 2Ψ components of surface wave phase-velocities at various periods for comparison with seismological results. As geodynamic models, we first consider motions of the plates on the surface as represented in rigid plate models such as

Table 1. Seismological and geodynamic models considered. APM: Absolute plate motion model, that is, assuming plate motions indicate shearing with respect to a stagnant lower mantle. *GP*, *GPT* and *GPT-VV* incorporate proper computation of mantle flow.

Abbreviation	Model type	Reference
E	Rayleigh wave phase velocity model, spline parametrization	Ekström (2001)
TW	Rayleigh wave phase velocity model, GSH parametrization	Trampert & Woodhouse (2003)
CLASH	Rayleigh wave phase velocity model, irregular parametrization	Beucler & Montagner (2006)
DKP	*SV* inversion, 3-D model, irregular parametrization	Debayle *et al.* (2005)
HS2	APM model, plate velocities in HS2 hotspot reference frame	Gripp & Gordon (1990)
NNR	APM model, plate velocities in NNR reference frame	Argus & Gordon (1991)
GP	Geodynamic 2Ψ estimate based on plate-motion related flow only	Becker *et al.* (2003, 2006a)
GPT	Geodynamic estimate based on plate-related flow and mantle density anomalies	Becker *et al.* (2003, 2006a)
GPT-VV	*GPT* model with lateral viscosity variations	Becker *et al.* (2006a), Becker (2006)

Table 2. Variance reduction (eq. 16) of best-fitting GSH representations of the irregularly parametrized seismological models at periods of 50 and 150 s. Values close to 100 per cent indicate that most spatial model information is contained in degrees $\leq L$.

Type	Variance reduction (per cent)					
	L = 8					
		$T = 50$ s			$T = 150$ s	
	E	$CLASH$	DKP	E	$CLASH$	DKP
A_0	83	65	65	69	53	51
2Ψ	57	67	34	50	76	41
4Ψ	30	30	–	24	33	–
	L = 20					
A_0	96	94	89	92	89	83
2Ψ	92	98	83	90	99	85
4Ψ	81	92	–	81	92	–

NUVEL1 (DeMets *et al.* 1990). In tectonic interpretations of seismic anisotropy it is often assumed that flow alignment of olivine will lead to a match of fast propagation directions (2Ψ signal) with such velocities (absolute plate motion, APM, hypothesis, e.g. Vinnik *et al.* 1992) (*cf*. Trampert & Woodhouse 2003). The idea is that plates shear the asthenosphere in a simple deformation pattern with regard to a static lower mantle. We know that mantle flow at depth is likely quite different from the direction of the surface motions, and that LPO formation is more complicated than plate-scale shear. However, we still include APM models since they are commonly found in the shear wave splitting literature. We use NUVEL1 motions in a no-net-rotation (*NNR*; Argus & Gordon 1991) and in the HS2 hotspot reference frame (*HS2*; Gripp & Gordon 1990). No seismological data were used in the derivation of these models.

Given the general patterns of azimuthal anisotropy from surface waves (Fig. 1), we expect APM type models to provide an adequate, zeroth-order approximation of deterministic patterns, particularly in oceanic plate regions. Against this simple tectonic hypothesis, we also consider geodynamic models that incorporate estimates of global mantle flow in 3-D, spherical mantle geometry. Following Becker *et al.* (2003), we compare model characteristics for mantle flow that incorporates the stirring effect of observed plate motions only (*GP*), and for mantle flow that also includes the driving effect of density anomalies (*GPT*) as inferred from isotropic seismic tomography. We use the composite model *SMEAN* by Becker & Boschi (2002) as a reference for long wavelength, global isotropic v_S structure. *SMEAN* has been shown to yield better results than other tomographic models with regard to several geophysical observables (Becker *et al.* 2003; Steinberger & Calderwood 2006). For the *GPT* models, seismological data thus enters as information on isotropic structure. For simplicity, we show geodynamic model results that are based on *SMEAN*, and not on upper mantle A_0 patterns from 3-D surface wave models such as Boschi & Ekström (2002) or *DKP*, which would be more consistent with our 2Ψ comparisons. However, tests using hybrid structure with A_0 from surface wave studies yielded very similar results.

The general methodology and other parameter choices are described in detail in Becker *et al.* (2003, 2006a). We use steady-state flow and advect tracers until a logarithmic, finite strain of 0.5 is reached at every sample location in the upper mantle where anisotropy is to be estimated. Values of order ∼0.5 for the strain were found to be required to match the observed variety in LPO textures in mantle xenoliths (Becker *et al.* 2006a). Becker *et al.* (2003) compared seismic anisotropy with the orientations of the extensional finite-strain axes. Here, anisotropy is computed from

the full elastic tensor using LPO fabric estimates for an olivine-enstatite mix from Kaminski *et al.*'s (2004) method (Becker *et al.* 2006a,b). Comparisons with the surface wave models are then computed by kernel-averaging the full 3-D anisotropic upper mantle. *GP* and *GPT* are based on flow with radially varying viscosity only; *GPT-VV* is like *GPT* but includes the effects of temperature and stress-dependent viscosity as well as stiff continental keels (similar to $\eta(T, \dot{\varepsilon})$ of Becker 2006). *GPT-VV* is here included as an example computation with plausible lateral viscosity variations (LVVs).

In our earlier work, we found that models like *GPT* which include active upwellings and downwellings lead to smaller misfits than *GP*, or APM models when compared with Ekström's (2001) inversions based on average, angular 2Ψ misfit and a simpler method of estimating anisotropy from flow (Becker *et al.* 2003). The importance of density driven flow was also pointed out by Behn *et al.* (2004) using shear wave splitting measurements.

4 RESULTS AND DISCUSSION

4.1 Heterogeneity wavelength spectra

Fig. 2 shows power spectra for A_0 and 2Ψ structure in the seismological models for a period of 50 s. The character of the isotropic spectra (Fig. 2a) of the four models is similar, and roughly matches those of global isotropic tomography (e.g. Becker & Boschi 2002, fig. 2). (*DKP* shows somewhat higher A_0 power, which is related to the addition of 3SMAC crustal structure; without this correction, A_0 amplitudes are more similar to the other models.) The match of A_0 spectra between models is found for all periods, although absolute σ_l values are reduced by ∼0.1 for 150 s compared to 50 s.

The spectra of different models' anisotropic component are less consistent (Fig. 2b), indicating that this part of the solution is less robustly constrained, and more sensitive to inversion strategy (parametrization, regularization) and/or noise in the data. There are differences between *TW* and *E*'s dispersion databases at short periods (Ekström *et al.* 1997; van Heijst & Woodhouse 1999), and the corresponding isotropic phase velocity maps, though those are more pronounced for Love waves. *TW* use many major arc measurements which increases resolution in the southern hemisphere, and it is likely that differences in coverage and measurement strategies become more important when 2Ψ is to be imaged.

The decay of σ_l with l for 2Ψ is, by design, much faster for *TW* than for the other models. *TW* chose their damping based on F-type significance tests to restrict anisotropic power for Rayleigh waves to be limited to $l \lesssim 8$. As anticipated, the slope of the 2Ψ power spectra is less steep than for A_0. If we compute power-law decay exponents for $\sigma_l \propto l^{-\beta}$ from the slopes of a $\log - \log$ linear regression for $l \geq 2$, we find $\beta \sim 1.2$ for A_0(1.3, 1.1, 1.2 for *E*, *CLASH* and *DKP*, respectively) and $\beta \sim 0.9$ for 2Ψ (0.9, 1.1, 0.6 for *E*, *CLASH* and *DKP*). That is, there is typically relatively more shorter wavelength power in the anisotropic than in the isotropic signal (note square root in the definition of power σ, eq. 11). The 2Ψ spectra of *E* and *CLASH* are similar to those derived by depth averaging of *DKP*, which is interesting given the distinct data sets and modelling approaches. *CLASH* has less absolute 2Ψ power than *E* or *DKP*, which might be related to the different choice in reference model (Beucler & Montagner 2006).

These results raise the question if differences in isotropic and anisotropic power spectra are due to a real, dynamic effect, or if this is just a result of poorer constraints on 2Ψ. For isotropic anomalies, the heterogeneity spectra decay is broadly consistent between

(a)

(b)
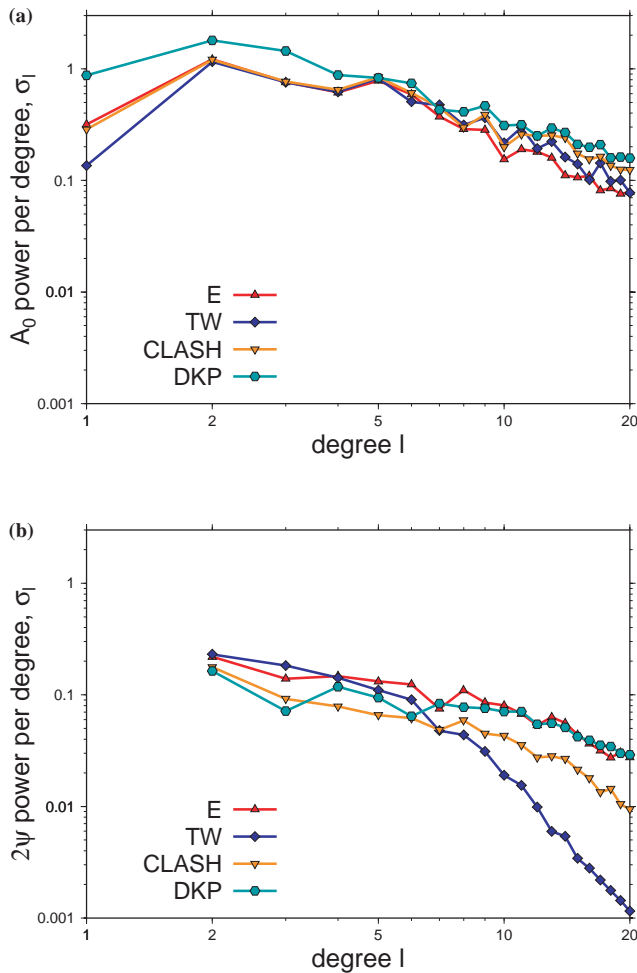
Figure 2. Power spectra of isotropic, A_0 (a), and azimuthally anisotropic, 2Ψ (b), structure in the seismological models for Rayleigh waves at 50 s; log $-$ log plot with ordinate units of percent anomaly with p normalization as in Section 2. *TW* was regularized by Trampert & Woodhouse (2003) to have little power for $l \gtrsim 8$. Compare Table 2, and see Table 1 for abbreviations and references.

different published models (Becker & Boschi 2002), but we may expect noise and incomplete coverage to have more of an effect on 2Ψ. Thermal convection computations have previously been used to make inferences on mantle convection by comparison with isotropic tomography's power spectra (e.g. Bunge *et al.* 1996; Tackley 1996). Here, we estimate the wavelength of heterogeneity that may be expected in 2Ψ azimuthal anisotropy. The flow computations we consider are long wavelength and deliberately simple. Among other effects, they do not include time-dependent convection, nor can we account for the complex tectonic history of continental regions. We therefore, expect geodynamic forward models to be most realistic in oceanic regions (*cf*. Becker *et al.* 2003, 2007). Time-dependent flow and small-scale convection will both serve to introduce shorter wavelength heterogeneity, making our synthetic 2Ψ spectra likely lower bounds.

Fig. 3, where we compare seismology- and geodynamics-based spectra (normalized by σ_2) of the 50 s Rayleigh wave 2Ψ component, confirms this suspicion: two APM spectra, derived from surface plate velocities in two different reference frames (*NNR* and *HS2*), show clearly a faster decay than *E* or *CLASH*. Differences in the reference frame (net rotation component) mostly affect structure
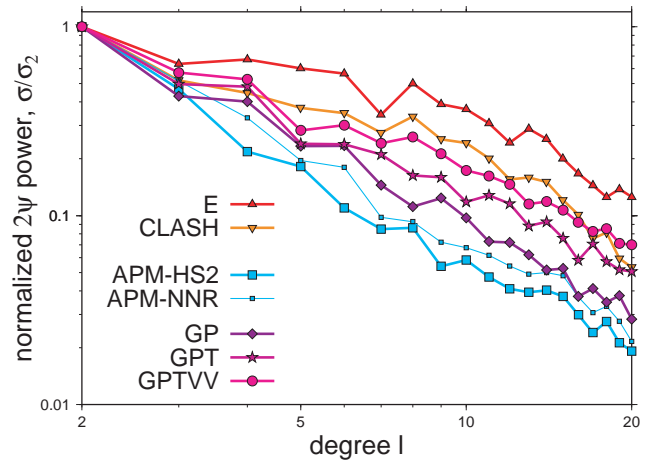
Figure 3. 2Ψ power normalized by σ_2, σ_l/σ_2, for seismological and geo-dynamic models at 50 s on a log $-$ log plot; see Table 1 for abbreviations.

in the lowest degrees, as expected. If we compute 2Ψ from the predicted LPO and elastic tensors of a mantle flow model that includes plate related currents only (*GP* in Fig. 3), the σ_l curve has slightly more medium wavelength content than APM models. This finding can be understood given that the geodynamic models employ a finite strain criterion so that textures are saturated. Such an approach will balance out the variations in strain-rates that result from different surface plate speeds. The larger plates, such as the Pacific, move fastest and so dominate the APM signal. If we normalize the *NNR* velocities and expand those fields, the predicted spectra are indeed very close to that for *GP*.

If buoyancy anomalies are included in the flow computations (*GPT* in Fig. 3), the decay of σ_l is less steep, as intraplate upwellings and downwellings now disturb the plate related shear and return flows. As expected from the analysis by Becker (2006), the further introduction of lateral viscosity variations with power-law and temperature-dependent viscosity (*GPT-VV*) amplify these variations. *GPT-VV* displays a spectral signal that is similar to *CLASH*, but still faster decaying than *E*. While detailed patterns in the geodynamic model spectra are moderately dependent on the modelling choices, the general behaviour as in Fig. 3 is robust and also found for longer Rayleigh-wave periods that sense deeper.

We conclude that the azimuthally anisotropic signal in models such as *E* and *CLASH* is consistent with the lower bound that large-scale geodynamic models can provide. From this we cannot infer that actual patterns are resolved by seismology or matched by geodynamics, as adding properly adjusted noise to the APM models would yield a similar effect. Given Trampert & Woodhouse's (2003) analysis and data set, we would indeed expect that we cannot say much about 2Ψ structure above $l \sim 8$. This leads to the issue of model correlations, to which we turn next.

4.2 Similarities and differences between models

4.2.1 Seismology

Fig. 4 shows the correlations per degree, r_l, for A_0 and 2Ψ for the three Rayleigh wave models; Table 3 lists and Fig. 5 displays the total correlation values for $r(8)$. We have chosen to quote most total correlations for the seismological models only up to $L = 8$ because this is the effective resolution of the longest wavelength 2Ψ model, *TW*.
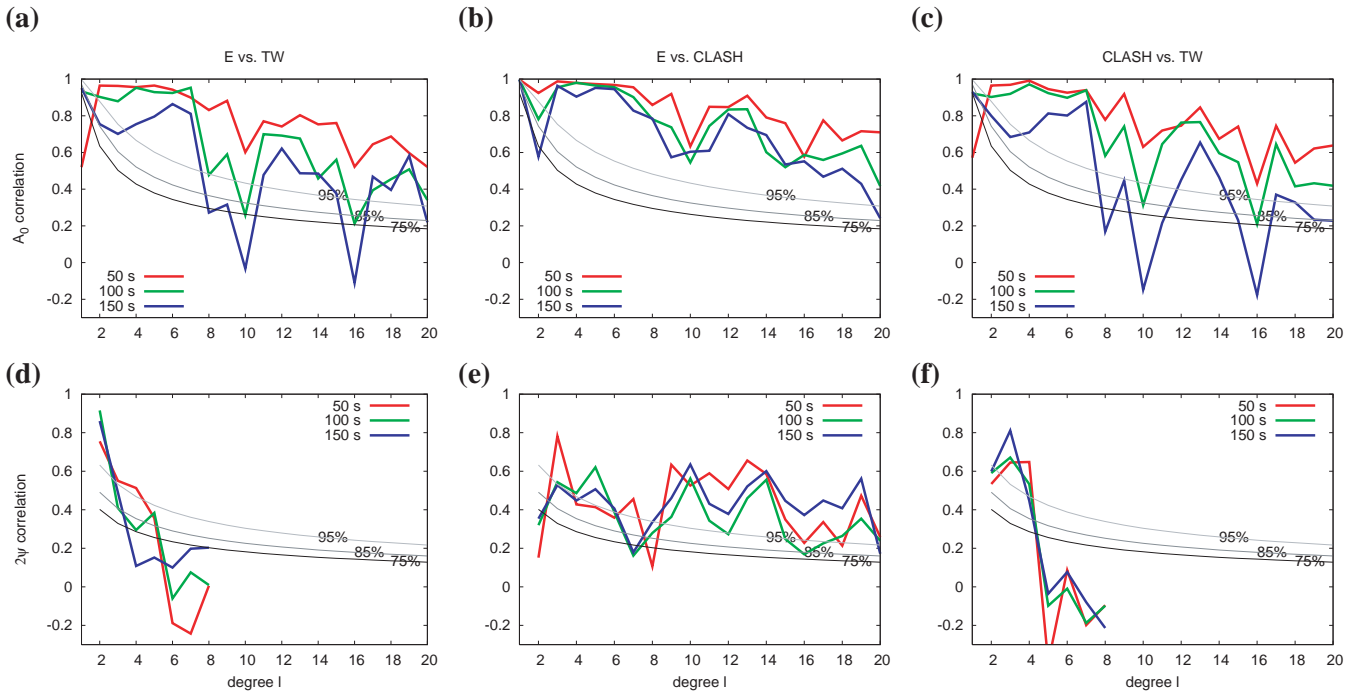
Figure 4. Correlation as a function of degree r_l, eq. (12), for isotropic, A_0, (a, b and c) and 2Ψ anisotropic (d, e and f) structure at periods between 50 and 150 s for the seismological models. We compare E and TW (a and d), E and $CLASH$ (b and e), and $CLASH$ and TW (c and f). Correlation plots are shown only up to $L = 8$ for 2Ψ from TW because of the effectively limited resolution due to damping choices. Confidence levels at 75, 85 and 95 per cent are plotted following Student's t distribution, eq. (13). Total correlation values for $L = 8$ are listed in Table 3 and displayed in Fig. 5.

Table 3. Total model correlations up to $L = 8$ for isotropic (A_0) and anisotropic (2Ψ) structure at intermediate, $T = 100$ s periods. The 99 per cent confidence level to be statistically different from random (Student's t) is $r(8) = 0.29$ and 0.21 for A_0 and 2Ψ, respectively. See also Fig. 5.

| | A_0 | | | |
	E	TW	$CLASH$	DKP
E	1.00	0.90	0.92	0.87
TW	0.90	1.00	0.91	0.85
$CLASH$	0.92	0.91	1.00	0.90
DKP	0.87	0.85	0.90	1.00

| | 2Ψ | | | |
	E	TW	$CLASH$	DKP
E	1.00	0.38	0.37	0.47
TW	0.38	1.00	0.35	0.24
$CLASH$	0.37	0.35	1.00	0.34
DKP	0.47	0.24	0.34	1.00

In general, isotropic structure correlates fairly well for all models, with $r(8) \sim 0.9$ and $r(20) \sim 0.8$ (Figs 4a–c and Table 3). These numbers are comparable to the correlations found by Becker & Boschi (2002) between whole-mantle, isotropic tomographic models, with, for example, $r(20) \sim 0.8$, on average, at a depth of 200 km, and much larger than the 99.9 per cent significance level ($r = 0.36$ for $L = 8$). However, as Fig. 4 shows, the match is wavelength dependent, and not similar for different model combinations. For example, TW does not match E or $CLASH$ well in A_0 for $l \sim 10$ and 16, which might be related to differences in the data on which the models are based. Such isotropic structure mismatch is also found at longer periods (Fig. 5).

The match between anisotropic 2Ψ structure is worse than for A_0 (Figs 4d–f); TW only significantly correlates with E or $CLASH$ at the longest wavelengths. The match between E and $CLASH$ is better, and above the 95 per cent significance level across most wavelengths, with peculiar decorrelation at degrees $\sim$2 and $\sim$8. The overall values of correlation are given in Table 3 for $r(8)$ and are of order 0.4 for most models ($r(20) \sim 0.3$). Interestingly, the correspondence between E and DKP is relatively good for 2Ψ at levels of $r(8) \sim 0.5$. We also find that patterns (GSH expansion of 2Ψ) show higher correlations than maximum amplitudes of 2Ψ anisotropy (SH expansion of the maximum 2Ψ contribution in eq. 1). The latter $r(8)$ correlations are only $\sim$0.3, compared to $\sim$0.4 as in Table 3.

The 4Ψ structure of E, $CLASH$ and TW correlates at $r(8) \sim 0.25$ ($\sim$0.15 less than $r(8)$ for 2Ψ) for 50 s periods, and becomes decorrelated ($r(8) \sim 0$) when TW is compared with E or $CLASH$ at 150 s. There, 4Ψ of E and $CLASH$ still match at $r(8) \sim 0.3$, which might indicate a deterministic signal, or could just be a consistent trade-off between different A_i terms.

While the anisotropic patterns are thus much more different between models than isotropic structure, there is still significant agreement for the 2Ψ component of some models (E, $CLASH$ and DKP). This analysis partially restates what is well known and can be inferred by visual comparison of published models: isotropic patterns are at present much better constrained than anisotropic patterns because the latter require better ray coverage. However, there is more agreement between models as stated by some. Overall model correlations and RMS ratios are shown in Fig. 5 for $L = 8$ for different periods. This comparison between results at different periods shows that both A_0 and 2Ψ structure is more similar between seismological models at shorter periods, illuminating shallower depth of the mantle. Fig. 5 also confirms that TW is different from $CLASH$ or E
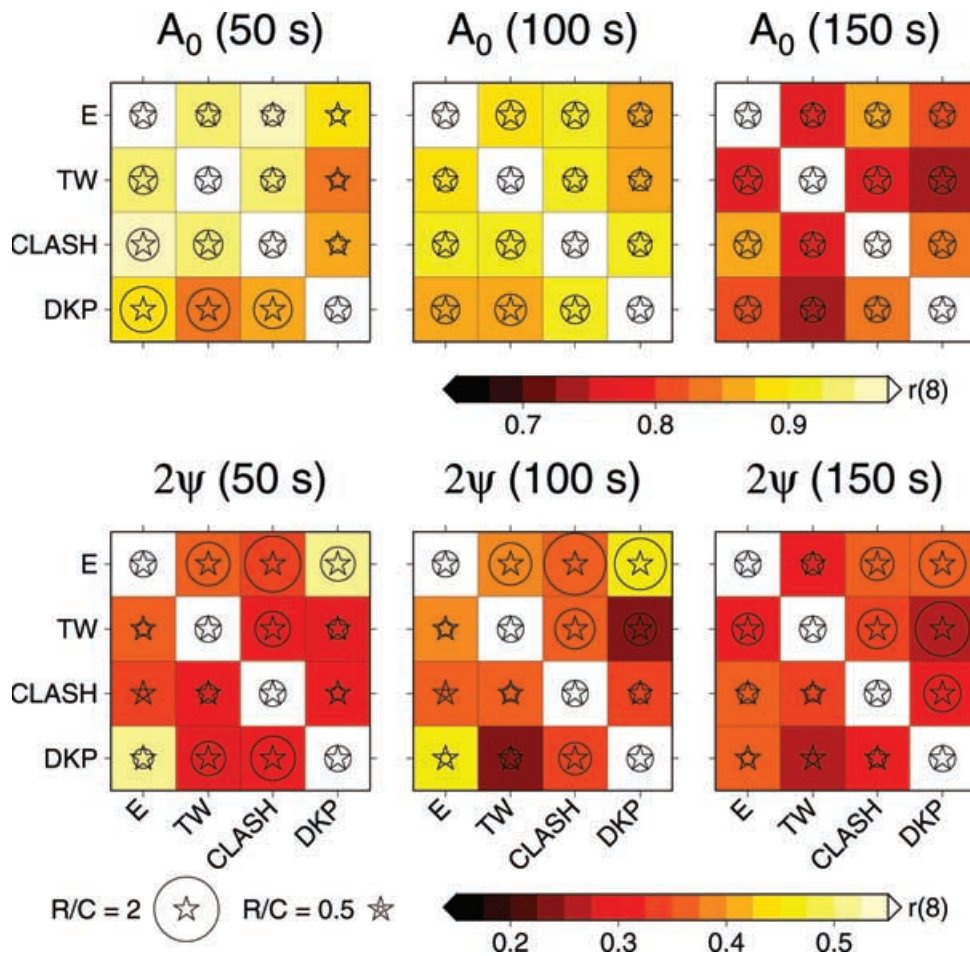
Figure 5. Total correlation (box shading) up to $L = 8$, $r(8)$, of seismological models. We show $r(8)$ for isotropic (top) and anisotropic (2Ψ terms, bottom row) phase velocity maps at periods of 50, 100, and 150 s. Also shown is the ratio of the total model (RMS) power up to $L = 8$; we indicate the RMS of the model in each row (R) divided by the RMS of the models in each column (C) by scaling the circle symbol size with this ratio compared to a fixed star. That is, circle smaller than star means that the row has smaller amplitude than the column model (see legend). Note different color scales for A_0 and 2Ψ, and see Table 1 for abbreviations.

not only in isotropic, but also in anisotropic structure (see, e.g. the 150 s plots).

Fig. 5 uses variable-size circle symbols to denote the ratio between global RMS values for the model listed in each row divided by the RMS values of the models in each column. That is, if the circle is smaller than the star symbol for a certain location, the row has smaller amplitude than the column model. The RMS ratios in Fig. 5 indicate that isotropic anomaly amplitudes are similar for all models. Small deviations in A_0 arise due to differently computed reference phase-velocity values (e.g. addition of 3SMAC to *DKP*) and are probably not significant. For 2Ψ, the RMS ratio varies more strongly between models, which is another reflection of the fact that anisotropic structure is less well resolved than isotropic patterns. This makes the inversion damping choices even more important (a notorious problem also for 4Ψ). That being said, we find that model *E* has more 2Ψ power than all other models for 50 and 100 s, and *CLASH* anomalies are of smaller amplitude than most other models at all periods.

We interpret these findings such that models *E*, *CLASH* and *DKP* show some similar anisotropic 2Ψ structure across a range of spatial scales, up to $L = 20$ or wavelengths of $\sim$2000 km. The actual correlation values are fairly small, and the origin of regional deviations and the higher degree match for $L \gtrsim 8$ clearly requires further study. However, this general, rough agreement is reassuring given that these models were derived from different sets of data. The finding that *TW* is dissimilar to *E* and *CLASH* for 2Ψ may be due to different input data. Alternatively, the mismatch may be related to the damping choices of *TW*, which penalizes high degree 2Ψ structure more strongly. The trade-off between A_0 and 2Ψ might then lead to a shift from anisotropic to isotropic anomalies to achieve similar variance reductions of the data. Only a systematic re-inversion of the different original data sets with consistent inversion schemes will allow us to untangle these issues, and such a study is the subject of a future publication.

Without *a priori* information, it is difficult to judge which is a more appropriate representation of Earth structure, as the wavelengths of spatial complexity of seismic anisotropy are poorly resolved at present. However, variations might continue down to individual geological units, or body wave Fresnel zone width (e.g. Fouch & Rondenay 2006; Becker *et al.* 2007). It is unclear how surface waves average over such heterogeneity, but at least some of the discrepancies of published models might be related to the mapping of small scale complexity to large scale A_0 and 2Ψ structure.
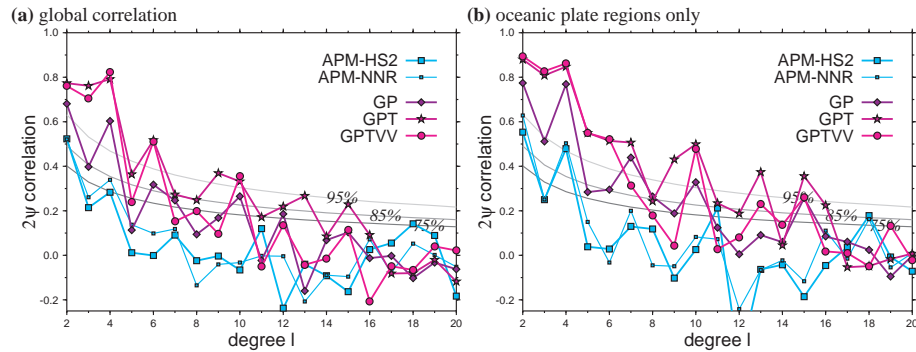
Figure 6. Correlation per degree, r_l, of geodynamic models with the 50 s 2Ψ model of Ekström (2001) (*cf*. Becker *et al.* 2003). We show r_l for global fields (a) and for comparisons where continental areas were smoothly set to zero before SH expansion (b, global significance levels as in a) shown for reference only). See Table 1 for abbreviations and Tables 4 and 5 for overall correlations.

4.2.2 Geodynamics

Returning to the question of the explanatory power of different geodynamic models, Fig. 6 shows r_l correlations for a comparison with Ekström's (2001) 50 s Rayleigh wave 2Ψ structure (model E). For tests of geodynamic models, we will focus on the full $L = 20$ representation as we have seen that at least some seismological models show consistent patterns throughout this range (e.g. Fig. 4e). We plot r_l in Fig. 6 both for a comparison of global structure, and for models where continental regions (from 3SMAC) were smoothly set to zero before GSH expansion. Confirming our earlier findings (Becker *et al.* 2003), we see that APM models are clearly outperformed by mantle circulation models, even at the longest wavelengths. This indicates that mantle flow models and olivine texture formation provide a better explanation for anisotropy than the simplified plate-shear assumption. Moreover, earlier models based on finite strain ellipsoids and the LPO texture-based patterns we analyse here yield similar results on large scales, as anticipated by Becker *et al.* (2006a).

The *GPT* model with buoyant upwellings and downwellings improves the fit compared to only plate-motion related flow (*GP*) further; the r_l is above the 75 per cent confidence level up to $l \sim 14$ for *GPT* (Fig. 6a). If we mask out continental structure, most correlations are shifted to higher values of r (Fig. 6b), but still fall below 75 per cent confidence at $l \sim 16$ (assuming that statistical significance is the same for Figs 6a and b). The restriction of the formal geodynamic model match to E for $l \lesssim 15$ might imply a limit to the effective spatial resolution of the geodynamic models in a systematic sense (input tomography plus model assumptions), but may well also indicate a limit in seismological resolution for anisotropy.

Tables 4 and 5 list the total global correlations up to $L = 20$ between different geodynamic models and Ekström's (2001) 50 and 150 s maps, as well as the correlations if we restrict the comparison to oceanic regions. The Tables also list the statistical significance levels associated with the difference between such values of $r(20)$, according to eq. (15). The best-fitting models from the examples as used in Tables 4 and 5 yield correlations around $r(20) \sim 0.5$. Such values can be considered good performance for large-scale geodynamic forward models; for example, inferred whole mantle slab structure matches tomography at levels of $r(20) \lesssim 0.4$ (Becker & Boschi 2002).

Reading off Table 4, we can see that the circulation model without density anomalies (*GP*) for 50 s as in Fig. 6 is significantly better than the *NNR* APM model at the 54 per cent level. Model *NNR* is typically better correlated with 2Ψ structure from E than *HS2*. This

Table 4. Total correlation $r(20)$ (second column) between geodynamic models of 2Ψ (listed in first column, acronyms explained in Table 1), and the 2Ψ component of tomographic model E. 'Null' indicates the null-hypothesis test for individual correlations being statistically significant. Other columns: For each couple of models, probability that the corresponding values of $r(20)$ be different from the reference value in the second column. We show results for globally evaluated models for periods of $T = 50$ and 150 s. Probabilities are evaluated using eq. (15) for comparisons of r^1 for each row with the r^2 of the model as specified in the column. Compare with Table 5.

| | | | $T = 50$ s | | | |
| | | | $1 - p(r^1 - r^2)$ | | | |
Model	r^i	Null	HS2	NNR	GP	GPT
Null	0.000	0.00				
HS2	0.177	0.82	0.00			
NNR	0.191	0.86	0.06	0.00		
GP	0.319	0.99	0.58	0.54	0.00	
GPT	0.453	1.00	0.90	0.89	0.60	0.00
GPT-VV	0.381	1.00	0.77	0.73	0.29	0.36

| | | | $T = 150$ s | | | |
| | | | $1 - p(r^1 - r^2)$ | | | |
Model	r^i	Null	HS2	NNR	GP	GPT
Null	0.000	0.00				
HS2	0.267	0.96	0.00			
NNR	0.250	0.95	0.08	0.00		
GP	0.257	0.95	0.05	0.03	0.00	
GPT	0.279	0.97	0.06	0.13	0.10	0.00
GPT-VV	0.212	0.90	0.24	0.17	0.20	0.30

may indicate some sensitivity to hotspot reference-frames, or net rotations, in the mapped azimuthal anisotropy. While the difference between the APM models is not statistically significant (Table 4), differences between various degrees of net rotations become more pronounced for *GPT* types of flow computations. This will be explored further in a future contribution.

The geodynamic model that includes density anomalies (*GPT*) is a further improvement on *NNR*, compared to *GP*, at the 60 per cent level (Table 4), confirming the conclusions of Becker *et al.* (2003) and Behn *et al.* (2004). Importantly, the ability of the geodynamic models to explain part of the structure in the seismological inversions for 2Ψ gives us confidence in the physical models for the lower-bound estimates of anisotropic heterogeneity power discussed above (Fig. 3).

For the particular LVV example from Becker (2006), Table 4 shows that the model fit to E for *GPT-VV* degrades compared to the

Table 5. Total correlation $r(20)$ as in Table 4 but limited to oceanic regions, continental structure has been set to zero before expansion. Significance levels computed as in Table 4 for simplicity.

| | | | $T = 50$ s, oceanic plate regions only | | | |
| | | | $1 - p(r^1 - r^2)$ | | | |
Model	r^i	Null	HS2	NNR	GP	GPT
Null	0.000	0.00				
HS2	0.240	0.94	0.00			
NNR	0.268	0.96	0.13	0.00		
GP	0.447	1.00	0.79	0.73	0.00	
GPT	0.579	1.00	0.97	0.96	0.66	0.00
GPT-VV	0.532	1.00	0.94	0.91	0.45	0.28
			$T = 150$ s, oceanic plate regions only			
			$1 - p(r^1 - r^2)$			
Model	r^i	Null	HS2	NNR	GP	GPT
Null	0.000	0.00				
HS2	0.323	0.99	0.00			
NNR	0.339	0.99	0.08	0.00		
GP	0.373	1.00	0.24	0.17	0.00	
GPT	0.415	1.00	0.43	0.36	0.21	0.00
GPT-VV	0.258	0.95	0.30	0.37	0.51	0.66

radially stratified viscosity computations, for example, *GPT* (see also Fig. 6). However, the drop in correlation from *GPT* to *GPT-VV* flow with LVVs is significant only at a low, 35 per cent level, and is model-dependent. We note that models *GP* and *GPT* already include the important toroidal flow component of mantle circulation, since plate velocities are prescribed at the surface. Differences in flow for models with and without LVVs are thus more subtle, and include the induction of net rotations at depth for *GPT-VV*, even though surface velocities are in the NNR reference frame for all models (Becker 2006).

The results of Fig. 6, therefore, do not mean that we can use correlations with azimuthal anisotropy as a firm constraint on the degree of LVVs at this point, and it is important to better understand which regions affect the global model misfit. Previous work also showed ambiguities in the effects of LVVs. For some density models, misfits were improved, for others degraded (Becker *et al.* 2006a,b). Conrad *et al.* (2007) explored an *SKS* data set similar to that used by Behn *et al.* (2004) and found that LVVs led to a slight improvement in misfit.

Table 4 also shows that deeper sensing Rayleigh waves with 150 s period for *E* are less well fit by the circulation models (100 s periods (not shown) are intermediate in performance). However, when correlations are limited to oceanic regions (Table 5), *r* is improved compared to the global models, from $r(20) \sim 0.5$ to ~ 0.6 for *GPT* and azimuthal anisotropy at 50 s. Moreover, the differences between the model fit to 50 and 150 s structure are less pronounced for the oceanic regions. In contrast, when the comparison is limited to continental regions (not shown), $r(20)$ drops to ~ 0.1 for *GPT*. These findings confirm our earlier results that flow models are more successful in explaining the oceanic plate signal, which may be expected given the complex tectonic history of the continents (*cf.* Becker *et al.* 2007).

Debayle *et al.* (2005) suggested that asthenospheric shearing may be more important in deeper regions underneath continents, while the shallower structure may be predominantly due to frozen-in anisotropy. Confirming their suggestion, we find that that deeper sensing waves at 150 s are indeed better correlated with the flow models underneath continents than the shallower sensing 50 s waves

($r(8)$ is improved from 0.13 to 0.34), and there is some preference for the LVV models in continents. However, we postpone further exploration of the regionalized partitioning of different anisotropy formation mechanisms, which is related to the question of the role of LVVs, until the robustness of the seismological models is understood better.

The correlation of geodynamic models and *CLASH* is lower than the correlation with *E*, with $r(20)$ dropping to ~ 0.2 globally, and ~ 0.3 in oceanic regions, for *GPT* at 50 s. While the 2Ψ structure in *CLASH* and *E* is fairly highly correlated in an overall, statistical sense for $L = 20$ (Table 3), the lower degrees up to $l \sim 8$ are relatively less similar in these models (Fig. 4e). Given that the geodynamic models fit degrees $l \lesssim 15$ best (Fig. 6), this indicates the importance of long wavelength structure.

If we repeat the analysis of correlation of flow computations with *TW*, *r* values are slightly smaller than for *E*, but the difference is much reduced from the drop compared to *CLASH*. For the *GPT* model, $r(20)$ drops by ~ 0.05 from *E* to *TW*, while $r(20)$ values are improved by ~ 0.05 for the *GP* models at 50 s. Using oceanic 2Ψ patterns from *TW* at 50 s instead of *E* as ground truth, we confirm that the geodynamic models do significantly better than APM, but *r* for *GPT* is not much better than *GP* ($r = 0.54$ and 0.56, respectively). Similar results are obtained for *DKP*, at 50 s *GPT* is better than any APM model at the ~ 85 per cent level, but the performance increase when adding density contributions ($r = 0.45$ versus $r = 0.39$) is only at the ~ 30 per cent level.

In summary, the general results from comparisons of 2Ψ structure with geodynamic models (density driven-flow improves the fit, and models work best in oceanic regions) are confirmed for all seismological models. Details such as correlation values and levels of significance, however, depend on the models. While such global comparisons are useful, the difference in model behaviour on several spatial scales needs to be explored further with regionalized comparisons that should also take into account variations in seismological model resolution.

5 CONCLUSIONS

While there are large discrepancies between published models of azimuthal anisotropy, there is also common mapped structure up to degree $L \sim 20$, corresponding to wavelengths of ~ 2000 km. Such agreement has been disputed before, and is an encouraging result for deterministic efforts of explaining seismic anisotropy based on mantle dynamics. Phase velocity maps that disagree with regard to Earth structure do so for both the isotropic and anisotropic signal. This points to the potential role of trade-offs between these model parameters, a well known problem that may, however, be addressed with the new *a priori* constraints we provide on the spectral character of azimuthal anisotropy. Our lower bound estimates of physically reasonable heterogeneity in this signal should be of help in future efforts to map the upper mantle. Global geodynamic flow models with active upwellings and downwellings do a significantly better job in explaining the mapped structure than the commonly used absolute plate motion hypothesis.

REFERENCES

Anderson, D.L. & Dziewoński, A.M., 1982. Upper mantle anisotropy: evidence from free oscillations, *Geophys. J. R. astr. Soc.,* **69,** 383–404.

Argus, D.F. & Gordon, R.G., 1991. No-net-rotation model of current plate velocities incorporating plate motion model NUVEL-1, *Geophys. Res. Lett.,* **18,** 2039–2042.

Becker, T.W., 2006. On the effect of temperature and strain-rate dependent viscosity on global mantle flow, net rotation, and plate-driving forces, *Geophys. J. Int.,* **167,** 943–957.

Becker, T.W. & Boschi, L., 2002. A comparison of tomographic and geodynamic mantle models, *Geochem., Geophys., Geosyst.,* **3,** doi:2001GC000168.

Becker, T.W., Browaeys, J.T. & Jordan, T.H., 2007. Stochastic analysis of shear wave splitting length scales, *Earth Planet. Sci. Lett.,* **259,** 526–540.

Becker, T.W., Chevrot, S., Schulte-Pelkum, V. & Blackman, D.K., 2006. Statistical properties of seismic anisotropy predicted by upper mantle geodynamic models, *J. Geophys. Res.,* **111** (B08309, doi:10.1029/2005JB004095).

Becker, T.W., Kellogg, J.B., Ekström, G. & O'Connell, R.J., 2003. Comparison of azimuthal seismic anisotropy from surface waves and finite-strain from global mantle-circulation models, *Geophys. J. Int.,* **155,** 696–714.

Becker, T.W., Schulte-Pelkum, V., Blackman, D.K., Kellogg, J.B. & O'Connell, R.J., 2006. Mantle flow under the western United States from shear wave splitting, *Earth Planet. Sci. Lett.,* **247,** 235–251.

Behn, M.D., Conrad, C.P. & Silver, P.G., 2004. Detection of upper mantle flow associated with the African Superplume, *Earth Planet. Sci. Lett.,* **224,** 259–274.

Beucler, É. & Montagner, J.-P., 2006. Computation of large anisotropic seismic heterogeneities (CLASH), *Geophys. J. Int.,* **165,** 447–468.

Boschi, L. & Ekström, G., 2002. New images of the Earth's upper mantle from measurements of surface-wave phase velocity anomalies, *J. Geophys. Res.,* **107**.

Boschi, L. & Woodhouse, J.H., 2006. Surface wave ray tracing and zimuthal anisotropy: generalized spherical harmonic approach, *Geophys. J. Int.,* **164,** 569–578.

Bunge, H.-P., Richards, M.A. & Baumgardner, J.R., 1996. Effect of depth-dependent viscosity on the planform of mantle convection, *Nature,* **379,** 436–438.

Conrad, C.P., Behn, M.D. & Silver, P.G., 2007. Global mantle flow and the development of seismic anisotropy: differences between the oceanic and continental upper mantle, *J. Geophys. Res.,* **112,** doi:10.1029/2006JB004608.

Dahlen, F.A. & Tromp, J., 1998. *Theoretical Global Seismology,* Princeton University Press, Princeton, New Jersey.

Debayle, E., Kennett, B.L.N. & Priestley, K., 2005. Global azimuthal seismic anisotropy and the unique plate-motion deformation of Australia, *Nature,* **433,** 509–512.

Debayle, E. & Sambridge, M., 2004. Inversion of massive surface wave data sets: model construction and resolution assessment, *J. Geophys. Res.,* **109,** B02316, doi:10.1029/2003BJ00265.

DeMets, C., Gordon, R.G., Argus, D.F. & Stein, S., 1990. Current plate motions, *Geophys. J. Int.,* **101,** 425–478.

Dziewoński, A.M. & Anderson, D.L., 1981. Preliminary reference Earth model, *Phys. Earth Planet. Inter.,* **25,** 297–356.

Ekström, G., 2001. Mapping azimuthal anisotropy of intermediate-period surface waves (abstract), *EOS Trans. AGU,* **82**(47), S51E–06.

Ekström, G., 2006. A simple method of representing azimuthal anisotropy on a sphere, *Geophys. J. Int.,* **165,** 668–671.

Ekström, G., Tromp, J. & Larson, E., 1997. Measurements and global models of surface wave propagation, *J. Geophys. Res.,* **102,** 8137–8157.

Forsyth, D.W., 1975. The early structural evolution and anisotropy of the oceanic upper mantle, *Geophys. J. R. astr. Soc.,* **43,** 103–162.

Fouch, M.J. & Rondenay, S., 2006. Seismic anisotropy beneath stable continental interiors, *Phys. Earth Planet. Inter.,* **158,** 292–320.

Gaboret, C., Forte, A.M. & Montagner, J.-P., 2003. The unique dynamics of the Pacific Hemisphere mantle and its signature on seismic anisotropy, *Earth Planet. Sci. Lett.,* **208,** 219–233.

Gripp, A.E. & Gordon, R.G., 1990. Current plate velocities relative to the hotspots incorporating the NUVEL-1 global plate motion model, *Geophys. Res. Lett.,* **17,** 1109–1112.

Hess, H.H., 1964. Seismic anisotropy of the uppermost mantle under oceans, *Nature,* **203,** 629–631.

Kaminski, É., Ribe, N.M. & Browaeys, J.T., 2004. D-Rex, a program for calculation of seismic anisotropy due to crystal lattice preferred orientation in the convective upper mantle, *Geophys. J. Int.,* **157,** 1–9.

Larsen, E.W.F., Tromp, J. & Ekström, G., 1998. Effects of slight anisotropy on surface waves, *Geophys. J. Int.,* **132,** 654–666.

Laske, G. & Masters, G., 1998. Surface-wave polarization data and global anisotropic structure, *Geophys. J. Int.,* **132,** 508–520.

Mochizuki, E., 1986. The free oscillations of an anisotropic and heterogeneous earth, *Geophys. J. R. astr. Soc.,* **86,** 167–176.

Montagner, J.-P. & Guillot, L., 2000. Seismic anisotropy in the Earth's mantle, in *Problems in Geophysics for the New Millenium,* pp. 217–253, eds Boschi, E., Ekström, G. & Morelli, A., Istituto Nazionale di Geofisica e Vulcanologia, Editrice Compositori, Bologna, Italy.

Montagner, J.-P. & Jobert, N., 1988. Vectorial tomography. II: application to the Indian Ocean, *Geophys. J. Int.,* **94,** 309–344.

Montagner, J.-P. & Nataf, H.-C., 1986. A simple method for inverting the azimuthal anisotropy of surface waves, *J. Geophys. Res.,* **91,** 511–520.

Montagner, J.-P. & Tanimoto, T., 1991. Global upper mantle tomography of seismic velocities and anisotropies, *J. Geophys. Res.,* **96,** 20337–20351.

Nataf, H.-C. & Ricard, Y., 1996. 3SMAC: an *a priori* tomographic model of the upper mantle based on geophysical modeling, *Phys. Earth Planet. Inter.,* **95,** 101–122.

Phinney, R.A. & Burridge, R., 1973. Representation of the elastic-gravitational excitation of a spherical Earth model by generalized spherical harmonics, *Geophys. J. R. astr. Soc.,* **34,** 451–487.

Press, W.H., Teukolsky, S.A., Vetterling, W.T. & Flannery, B.P., 1993. Numerical recipes in *C: The Art of Scientific Computing,* 2nd edn, Cambridge University Press, Cambridge.

Romanowicz, B. & Snieder, R., 1988. A new formalism for the effect of lateral heterogeneity on normal modes and surface waves. II. General anisotropic perturbation, *Geophys. J.,* **93,** 91–99.

Sieminski, A., Liu, Q., Trampert, J. & Tromp, J., 2007. Finite-frequency sensitivity of surface waves to anisotropy based upon adjoint methods, *Geophys. J. Int.,* **168,** 1153–1174.

Smith, M.L. & Dahlen, F.A., 1973. The azimuthal dependence of Love and Rayleigh wave propagation in a slightly anisotropic medium, *J. Geophys. Res.,* **78,** 3321–3333.

Smith, M.L. & Dahlen, F.A., 1975. Correction to 'The azimuthal dependence of Love and Rayleigh wave propagation in a slightly anisotropic medium', *J. Geophys. Res.,* **80,** 1923.

Smith, D.B., Ritzwoller, M.H. & Shapiro, N.M., 2004. Stratification of anisotropy in the Pacific upper mantle, *J. Geophys. Res.,* **109,** doi:10.1029/2004JB003200.

Steinberger, B. & Calderwood, A., 2006. Models of large-scale viscous flow in the earth's mantle with constraints from mineral physics and surface observations, *Geophys. J. Int.,* **167,** 1461–1481.

Tackley, P.J., 1996. Effects of strongly variable viscosity on three-dimensional compressible convection in planetary mantles, *J. Geophys. Res.,* **101,** 3311–3332.

Tanimoto, T. & Anderson, D.L., 1984. Mapping convection in the mantle, *Geophys. Res. Lett.,* **11,** 287–290.

Tanimoto, T. & Anderson, D.L., 1985. Lateral heterogeneity and azimuthal anisotropy of the upper mantle: love and Rayleigh waves 100–250 s, *J. Geophys. Res.,* **90,** 1842–1858.

Trampert, J. & Woodhouse, J.H., 1995. Global phase velocity maps of Love and Rayleigh waves between 40 and 150 seconds, *Geophys. J. Int.,* **122,** 675–690.

Trampert, J. & Woodhouse, J.H., 2003. Global anisotropic phase velocity maps for fundamental mode surface waves between 40 and 150 s, *Geophys. J. Int.,* **154,** 154–165.

van Heijst, H.J. & Woodhouse, J.H., 1999. Global high-resolution phase velocity distributions of overtone and fundamental-mode surface waves determined by mode branch stripping, *Geophys. J. Int.,* **137,** 601–620.

Vinnik, L.P., Farra, V. & Romanowicz, B., 1989. Azimuthal anisotropy in the Earth from observations of *SKS* at Geoscope and Nars broadband stations, *Bull. Seismol. Soc. Am.,* **79,** 1542–1558.

Vinnik, L.P., Makeyeva, L.I., Milev, A. & Usenko, Y., 1992. Global patterns of azimuthal anisotropy and deformation in the continental mantle, *Geophys. J. Int.,* **111,** 433–447.

Wessel, P. & Smith, W.H.F., 1991. Free software helps map and display data, *EOS Trans. AGU,* **72,** 445–446.

Zhang, Y.S. & Lay, T., 1996. Global surface wave phase velocity variations, *J. Geophys. Res.,* **101,** 8415–8436.